Nanoscale Res Lett (2007) 2:410–415
DOI 10.1007/s11671-007-9076-2

NANO EXPRESS

Physical Behavior of Nanoporous Anodic Alumina Using Nanoindentation and Microhardness Tests

Te-Hua Fang · Tong Hong Wang · Chien-Hung Liu · Liang-Wen Ji · Shao-Hui Kang

Received: 14 May 2007 / Accepted: 16 June 2007 / Published online: 19 July 2007

Abstract In this paper, the mechanical response and deformation behavior of anodic aluminum oxide (AAO) were investigated using experimental nanoindentation and Vickers hardness tests. The results showed the contact angle for the nanoporous AAO specimen was 105° and the specimen exhibited hydrophobic behavior. The hardness and the fracture strength of AAO were discussed and a three-dimensional finite element model (FEM) was also conducted to understand the nanoindentation-induced mechanism.

Keywords Nanoindentation · Anodic aluminum oxide (AAO) · Porosity · Hardness · Finite element method (FEM)

Introduction

Anodic aluminum oxide (AAO) has attracted much attention due to its excellent physical and chemical properties. This material can be applied in the field of catalysis, chemical/biosensors, templates for self-assembly, filters, nanofluidic transistors and humidity sensors [1–3]. Owing to its low cost and easy fabrication, an anodization technique is used to synthesize nanoporous AAO.

The size of the nanopores can be controlled by the voltages applied during anodization and the modulus and the hardness of nanoporous alumina has been shown to vary with the pore size [4]. The mechanical responses of the complicated network geometries of AAO can be simply measured by the size of couple pores, although it is difficult to predict the responses theoretically.

In this paper, we investigate the mechanical properties of nanoporous AAO using nanoindentation and microhardness tests. The mechanism and properties were determined and discussed by experimental measurement as well as finite element analysis (FEA).

Specimen Preparation

Nanoporous AAO was prepared electrochemically using a two-step anodization technique to achieve an oxide film with a regularly ordered porous structure. The first anodization was carried out until the residual Al film thickness approached the desired level, then the oxides were stripped away, and subsequently a second anodization was performed until the remaining Al samples were completed anodized. A Ti sheet was used as a cathode for the anodization of the Al samples under a constant voltage. The first anodization was performed using a 0.4 M oxalic acid solution at 20 °C and 50 V for 4 h, and then the oxides were removed by immersing the samples in a mixture of 2 wt.% chromic acid and 6 wt.% phosphoric acid at a temperature of 60 °C.

The desired thickness of the AAO films was obtained by a subsequent second anodization. After the second anodization, the AAO could be widened by increasing the

T.-H. Fang (✉) · S.-H. Kang
Institute of Mechanical and Electromechanical Engineering, National Formosa University, Yunlin 632, Taiwan
e-mail: fang.tehua@msa.hinet.net

T.-H. Fang · C.-H. Liu · L.-W. Ji
Institute of Electro-Optical and Materials Science, National Formosa University, Yunlin 632, Taiwan

T. H. Wang
Thermal Laboratory, Advanced Semiconductor Engineering, Inc., Kaohsiung 811, Taiwan

anodization time and concentration of the acid solution. For the pore widening process, the solution used was 0.1 M phosphoric acid solution at a temperature of 30 °C for about 1 h.

Results and Discussion

Structure and Surface Properties

Microstructures and surface properties of the samples were measured by using a scanning electron microscope (SEM, Hitachi S-3000N) and atomic force microscope (AFM, Veeco/TM CP-RII SPM system). Figure 1 shows the SEM image of the resultant AAO microstructure. The cylindrical open-pores penetrated the entire thickness of the samples. The hole-diameter of each pore was approximately 200 nm. It can be seen that the discriminable pores distributed macroscopically. The porosity of the specimen was about 60%.

Figure 2 shows the AFM image of the AAO. The image was obtained by using AFM with a TiN probe tip in the tapping mode. The radius of the probe tip was less than 20 nm. The average force constant and the resonance frequency were set at 34 N/m and 350 kHz, respectively. The measurements of the average roughness (Ra) and the mean-square-root roughness (RMS) of the specimen were 23.4 and 29.3 nm, respectively. The average height from peak to valley of the surface was 232.6 nm.

Wetting and Optical Behavior

In order to understand how the interfacial properties effect to the introduction of water molecules on the AAO, it is important to perform a careful study of the liquid–solid interfaces interactions. Here, the contact angle has been used as a measure of wetting between a liquid and a solid surface [5]. De-ionized (DI) water droplets with a total volume of 5 μL were made for the subsequent contact measurement. Figure 3 shows the side views of the DI water droplet on the surface of the AAO specimen. The contact angle for the nanoporous AAO was 105° as the structure presents a hydrophobic behavior.

The optical properties were studied with a Hitachi U-3310 spectrophotometer. The spectral reflection measurement for the AAO is shown in Fig. 4. The film reflection shows a significant drop from 60% to null near the wavelength 250 nm. This is because the nanoporous film exhibits a higher light scattering and therefore yields a broadband anti-reflectivity. This behavior enables broadband elimination of reflection for incident light from all directions when the wavelength is higher than 250 nm. Hiller et al. [6] also found nanoporous polymer films yield broadband anti-reflectivity.

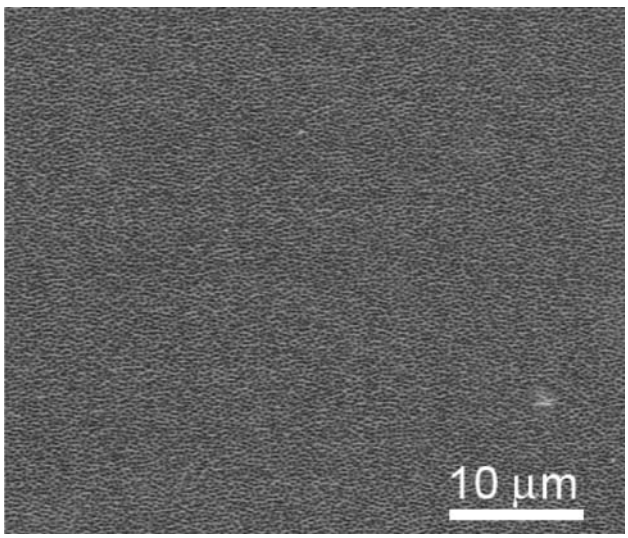

Fig. 1 SEM images of the plan view of nanoporous AAO

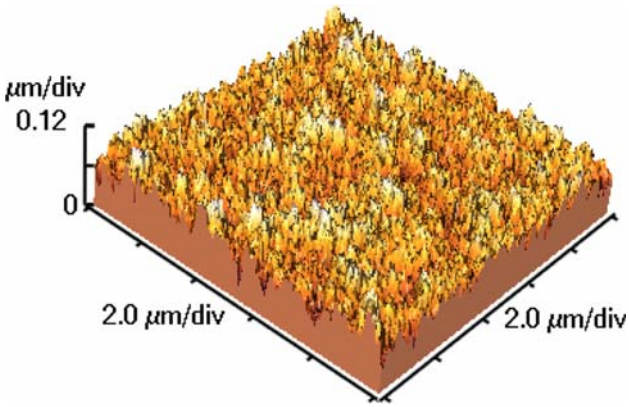

Fig. 2 AFM image of the AAO surface

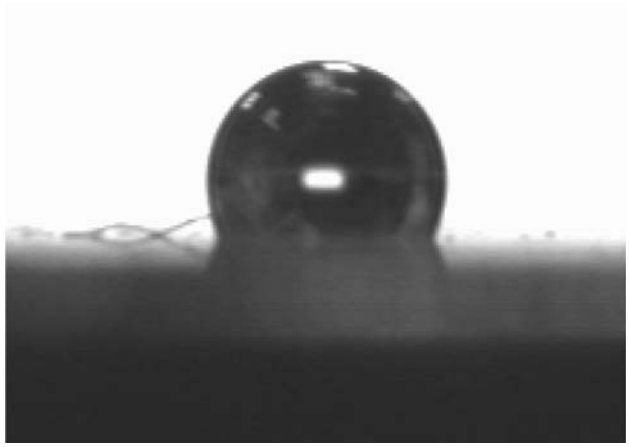

Fig. 3 Side view of the DI water droplet on the AAO nanoporous structure

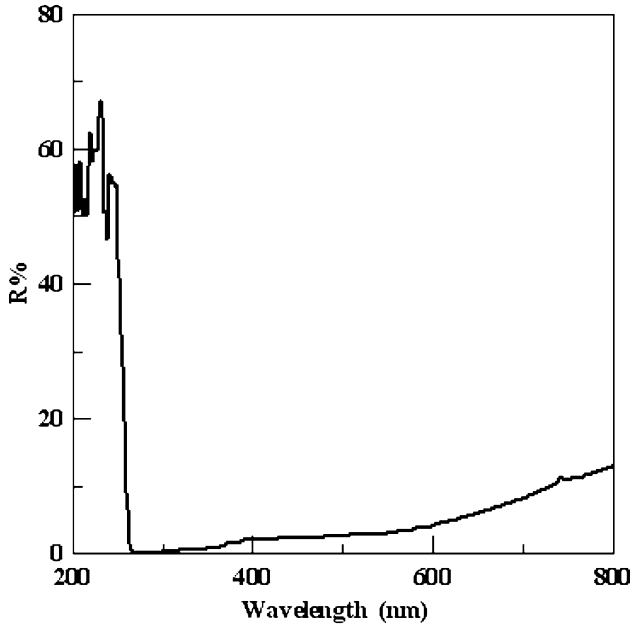

Fig. 4 Reflection of the AAO nanoporous structure

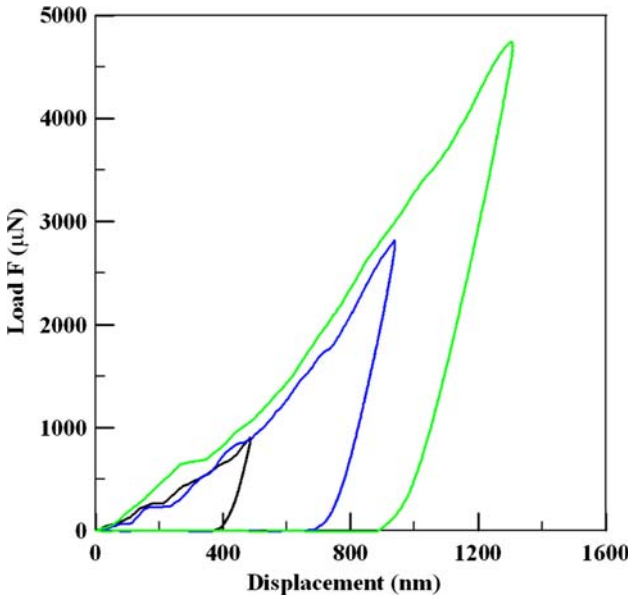

Fig. 5 L–D curves of the nanoporous AAO for different loads

Nanoindentation Response

Nanoindentation has been widely used for measuring nanomechanical properties such as the hardness and Young's modulus of test samples [7]. A Hysitron nanoindentation system equipped with a Berkovich diamond indenter with an approximately 200-nm-radius was used in this study. Figure 5 shows the corresponding load–displacement (L–D) curves of the AAO specimen at indentation loads of 1, 3 and 5 mN at room temperature. As the load increased, the penetration depth also increased. The results show that the pop-in behavior occurs at the beginning of the loading process. This behavior, which is different from the dislocation-slip phenomenon, is because the nanopore walls crash and collide with one another.

To further characterize the mechanical enhancements, we examined the hardness and Young's modulus of the AAO. Hardness is defined as the resistance to local deformation. It is expressed as the maximum indentation load, $P_{\max}$, divided by the real contact area, A_{real},

$$H = \frac{P_{\max}}{A_{\text{real}}(h)} \tag{1}$$

where the real contact area A_{real} could be defined as the contact area multiplied by the porosity of AAO. The contact area is a function of the contact depth, h.

The Young's modulus, E, of the test material can be obtained with the following equation [8],

$$E = (1 - v^2)\left[\frac{1}{E^*} - \frac{1 - v_i^2}{E_i}\right]^{-1} \tag{2}$$

where v is the Poisson's ratio of the test material while E_i and v_i denote Young's modulus and Poisson's ratio of the indenter, respectively. The indenter properties used in this study are E_i = 1,140 GPa and v_i = 0.07. E^* is the reduced modulus of the system and can further be defined as

$$E^* = \frac{\sqrt{\pi}}{2}\frac{S}{\beta\sqrt{A_{\text{real}}}} \tag{3}$$

where S is the stiffness of the test material, which can be determined from the slope of the initial unloading by

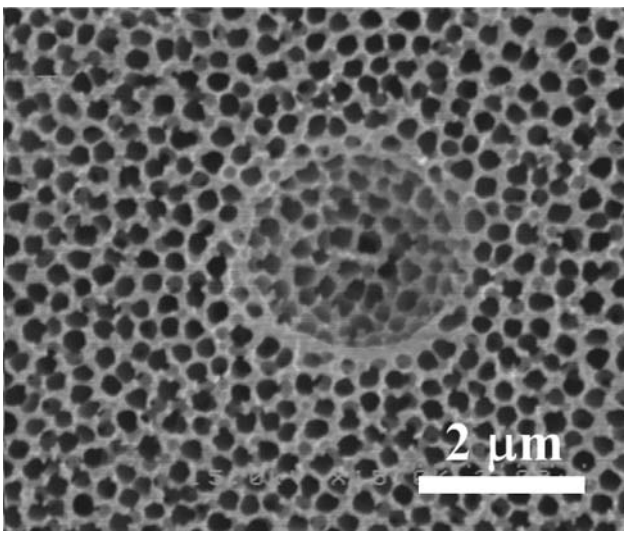

Fig. 6 SEM image of the indent mark of the AAO using a Berkovich indenter

evaluating the maximum load and the maximum depth, where $S = dP/dh$. β is a shape constant of the indenter, which is 1.034 for the Berkovich tip.

The nanohardness for the AAO ranged between 270 MPa and 310 MPa. The Young's modulus of the nanoporous AAO for indentation depths of about 400–1,200 nm are 3.1–7.2 GPa. Moreover, the low modulus of the samples is probably associated with the absorbed moisture or residual water from the anodizing process [9]. It is also interesting to note that the hardness and the Young's modulus demonstrated here are considerably lower than those found elsewhere [4] because of the pore diameter is larger than in the other study. Certainly, besides structural differences, mechanical effects are another possible reason for the low hardness and Young's modulus. Figure 6 shows the SEM image of an indented mark after nanoindentation. The porous structure leads to a deformation mechanism via crushed pores although the solid barrier layer did partially mitigate the crushed pores beneath the indenter.

Microhardness Test

The microhardness test used a Vickers diamond tip, with the shape of square-based pyramid with an angle of 136° between opposite faces as an indenter. The Vickers hardness, Hv could be estimated by

$$Hv = \frac{P}{A} = 1.854\frac{P}{d^2} \tag{4}$$

where A is the projected surface area of the residual indent, P is the force applied to the diamond and d is the average

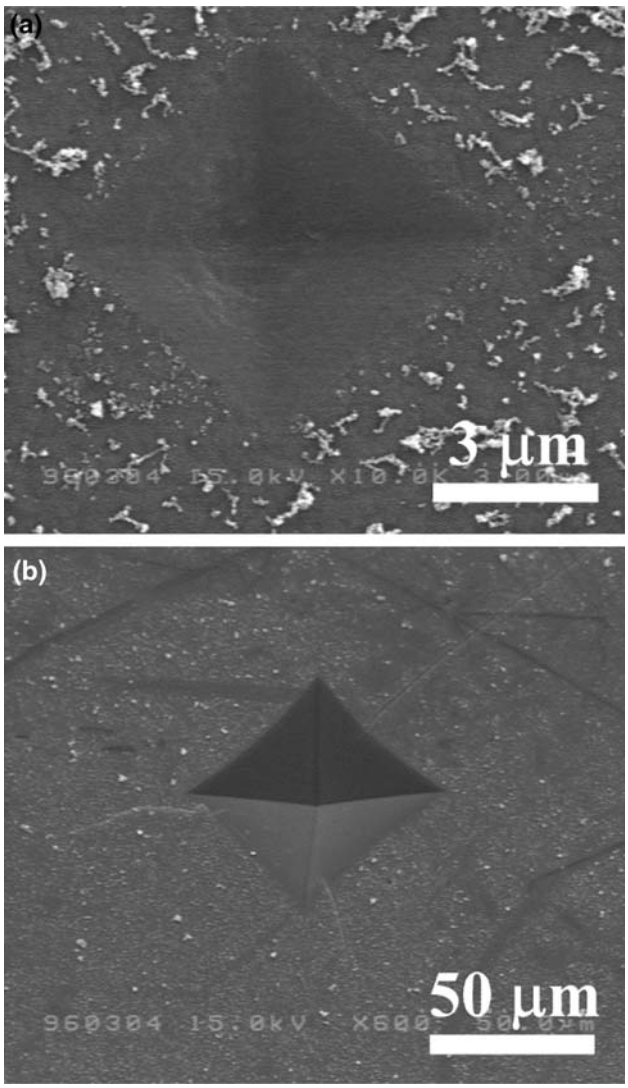

Fig. 7 SEM image of the indent mark of the AAO using a Vickers indenter after loads of (**a**) 50 g and (**b**) 1,000 g

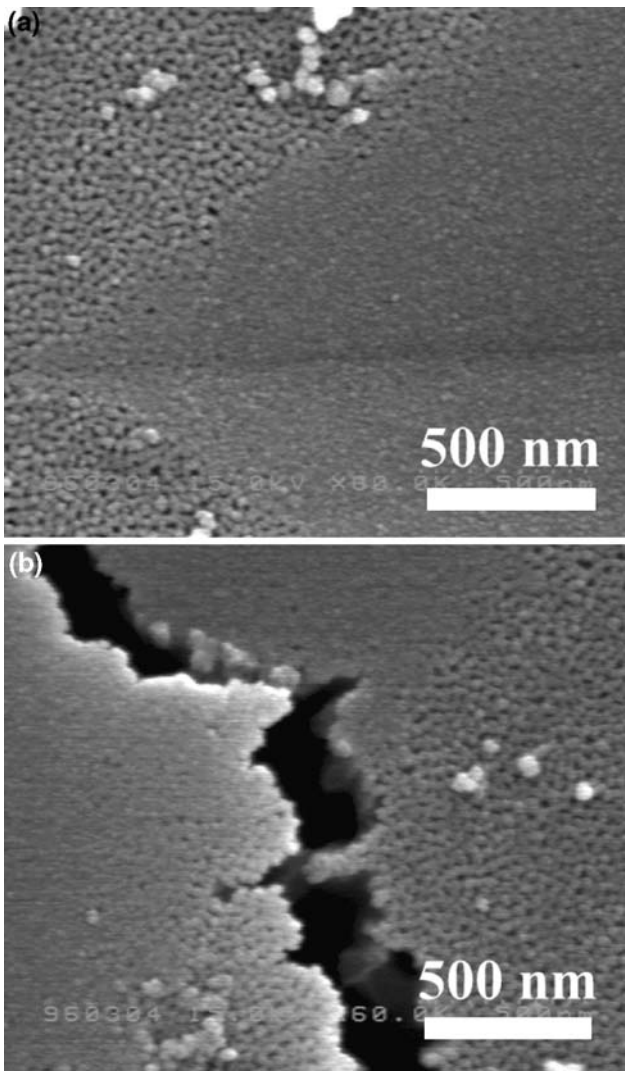

Fig. 8 Morphologies at the edge of the indented AAO after loads of (**a**) 5 g and (**b**) 1,000 g, respectively

indent length of the diagonal left by the indenter. In this study, the forces were set as 50, 100, 500 and 1,000 g. The time for the initial application of force was 5 s, and then the test force was maintained for another 15 s. The calculated hardness was between 0.3 GPa and 2.0 GPa. One may see that there is almost the same of hardness with the smallest load when compared to the nanoindentation results for the smallest indentation. However, with regard to the greatest load of microhardness test and the greatest depth of nanoindentation, their differences are significant. This was due to the substrate effect rebounding from this micro-scale test, while nanoindentation was only localized. On the other hand, if the aim is to obtain the intrinsic mechanical properties of this particular sample, mechanical loads ought to be small enough to prevent any substrate effect.

Figure 7a shows the SEM image of an indent of the AAO sample using a Vickers indenter with load of 50 g. These images demonstrate that the porous architecture was crushed during indentation. Figure 7b shows the SEM image of an indent of the AAO sample using a Vickers indenter with load of 1,000 g. When increasing the load until 1,000 g was applied to the AAO, the specimen suffered a fracture along the pore wall. It was observed that the crack in the vicinity of the indent.

The yield strength σ of the material could be approximated as:

$$\sigma = \frac{Hv}{c_v} \tag{5}$$

where c_v is a constant determined by geometrical factors usually ranging between 2 and 4. By the assumption that c_v is equal to 3, the calculated yield strengths of the specimen are 300 and 667 MPa for loads of 5 and 1,000 g, respectively. Figure 8a and b show the corresponding morphologies at the edge of the indented AAO after loads of 5 and 1,000 g, respectively. It is apparent that the load of 5 g leaves a faint impression without fracture, whereas the load of 1,000 g incurs an obvious crack which represents a brittle failure. The crack propagates along the solid barrier layer of the AAO.

FEA of Indentation

For the sake of understanding the mechanical behaviors of AAO under nanoindentation, FEA was carried out using the commercial finite element package ANSYS v. 10.0. Obviously, such a complex, hollow structure is not easy to

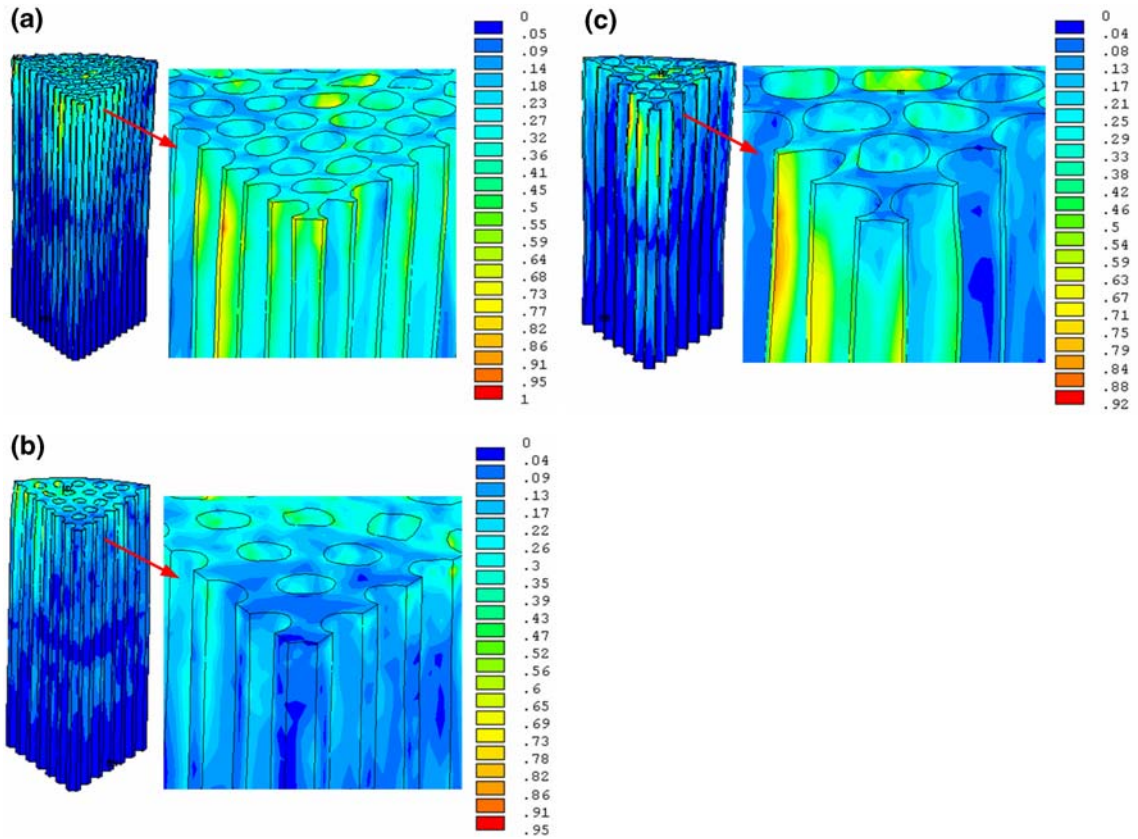

Fig. 9 Normalized von Mises stress distributions of the nanoporous AAO at the maximum load of pore diameters (**a**) 100 nm, (**b**) 150 nm and (**c**) 200 nm. Using the maximum von Mises stress of pore diameter 100 nm as the reference which is equal to 1

convergent with a nonlinear constitutive model. Due to this, the AAO was modeled as an elastically deformable solid which has a Young's modulus of 370 GPa, and a Poisson's ratio of 0.22 at room temperature, and the diamond Berkovich indenter was assumed to be a rigid solid. For the pyramidal characterization of the Berkovich indenter, the AAO and indenter were built as a sixth-symmetry finite element model. Three diameters of pores: 100, 150 and 200 nm was compared under the maximum indentation of 400 nm. Figure 9 shows the normalized von Mises stress distributions of the nanoporous AAO for different diameters of pores at the maximum load using the maximum von Mises stress of pore diameter of 100 nm as the reference, i.e. equal to 1. From the figures, it is seen that under identical indentation test conditions, the greater the pore diameter, the lower the normalized von Mises stress. This also means that larger pore of AAO would result in a lower stress-related properties, such as hardness and Young's modulus, which resembles our findings above.

Conclusion

In summary, we have demonstrated the wetting, optical and mechanical behaviors of nanoporous AAO. The contact angle of nanoporous AAO is over 90°, it exhibited hydrophobic behavior and the film reflection is lower than 20% when the wavelength between 300 nm and 800 nm. Both micro to nano-scale indentations were carried out to examine their mechanical behaviors. Since the diameter of these particular pores is in general greater than normal, both the hardness and the Young's modulus are comparatively small. FEA with an elastically deformable solid was used to model the AAO. Lower von Mises stress was found for AAO with larger pores, which resembled to experimental findings with regard to hardness and Young's modulus.

Acknowledgements This work was supported in part by the National Science Council of Taiwan under Grant No. NSC 95-2221-E150-066.

References

1. R.E. Benfield, D. Grandjean, M. Kroll, R. Pugin, T. Sawitowski, G. Schmid, J. Phys. Chem. B. **105**, 1961 (2001)
2. H. Yang, S. Rahman, Nano Lett. **3**, 439 (2003)
3. Z. Wang, M. Brust, Nanoscale Res. Lett. **2**, 34 (2007)
4. S. Ko, D. Lee, S. Jee, H. Park, K. Lee, W. Hwang, Thin Solid Films **515**, 1932 (2006)
5. R. Redon, A. Vazquez-Olmos, M.E. Mata-Zamora, A. Ordonez-Medrano, F. Rivera-Torres, J.M. Saniger, Rev. Adv. Mater. Sci. **11**, 79 (2006)
6. J. Hiller, J.D. Mendelsohn, M.F. Rubner, Nat. Mater. **1**, 59 (2002)
7. T.H. Fang, W.J. Chang, Microelectron. Eng. **65**, 231 (2003)
8. T.H. Fang, W.J. Chang, Appl. Surf. Sci. **252**, 6243 (2006)
9. J.C. Grosskreutz, J. Electrochem. Soc. **116**, 1232 (1969)